An Investigation of Charge Transfer at the Cluster-Substrate Interface Using Size-Selected Clusters

A Thesis Presented

by

Lizhou Nie

to

The Graduate School

in Partial Fulfillment of the

Requirements

for the Degree of

Master of Science

in

Chemistry

Stony Brook University

August 2013

UMI Number: 1546693

UMI

Dissertation Publishing

ProQuest®

Stony Brook University

The Graduate School

Lizhou Nie

We, the thesis committee for the above candidate for the

Master of Science degree, hereby recommend

acceptance of this thesis.

Michael G. White – Thesis Advisor
Professor, Department of Chemistry

José Rodriguez – Chairperson of Defense
Senior Chemist, Brookhaven National Laboratory

Jiangyong Jia – Third Member
Associate Professor, Department of Chemistry

This thesis is accepted by the Graduate School

Charles Taber
Interim Dean of the Graduate School

Abstract of the Thesis

An Investigation of Charge Transfer at the Cluster-Substrate

Interface Using Size-Selected Clusters

by

Lizhou Nie

Master of Science

in

Chemistry

Stony Brook University

2013

In order to improve performance of heterogeneous catalysts used in industrially important processes, it is of critical importance to understand the interfacial electronic properties of adsorbates on solid surfaces. Among various important electronic properties, interfacial charge transfer between the active catalyst and its supporting material can be correlated with the chemical activity of the catalyst for certain reactions. The work presented in this thesis, focuses on the charge transfer and surface dipole study at the interface of metal oxide/sulfide clusters deposited on Cu(111) and metal oxide clusters deposited on a Cu_2O/Cu(111) film, studied using two-photon photoemission (2PPE) spectroscopy and other surface analysis techniques. These materials represent models for nanocatalysts for alternative fuel production (hydrogen, methanol) through the water-gas-shift reaction and CO_2 hydrogenation.

Size-selected metal oxide clusters (Mo_3O_9, W_3O_9, Ti_3O_6, Mo_3O_6, W_3O_6 and Ti_5O_{10}) and metal sulfide cluster (Mo_4S_6) have been selectively deposited on Cu(111)

surface or a $Cu_2O/Cu(111)$ film, using a size-selection cluster deposition apparatus. Cluster distribution on the substrate was monitored with Auger electron spectroscopy (AES), and follows a Gaussian distribution within the different cluster-substrate systems. The work function shift due to cluster deposition was measured with 2PPE spectroscopy, which showed a consistent trend of work function increase for all the cluster-substrate systems here. In addition, surface dipoles are derived from work function shift measurement using the Topping model, which provides a method to study the interfacial charge transfer orientation and magnitude. These results suggest strong cluster-substrate interactions that result in interfacial charge transfer that is highly cluster and substrate dependent.

Table of Contents

List of Tables

List of Abbreviations

2PPE: Two-Photon Photoemission

AES: Auger Electron Spectroscopy

DC: Direct Current

HDS: Hydrodesulphurization

IS: Image State

LN_2: Liquid Nitrogen

RF: Radio Frequency

SHG: Second Harmonic Generation

SS: Surface State

THG: Third Harmonic Generation

TPD: Temperature Programmed Desorption

UHV: Ultrahigh Vacuum

WGS: Water Gas Shift

Acknowledgments

In my two-years of graduate study, I have received much help which has guided me through all the difficulties and made me grow up. This help has not only solved my problems, but will also be beneficial for me for the rest of my life. First and foremost, I would like to thank my parents, who are always there listening to me and supporting me. Your love and trust are always my strongest motivation to fight for a better and happier life for you and me. I would also like to thank my ex-girlfriend, who has spent more than three years loving and supporting me.

In addition, I would like to thank my advisor, Dr. Michael White, who not only patiently guided me in a research area I had no experience in before, but also has always been very considerate about my research and daily life and has given me a lot of precious advice. I would also like to thank my committee members, Dr. José Rodriguez and Dr. Jiangyong Jia for your valuable instruction on my research and scientific talk. Besides, as my compatriot and a lovable senior graduate student, Yixiong Yang has not only taught me all the important knowledge in the lab, but also pulled me out from the emotional whirlpool and made me stronger, which I will be grateful for my whole life. I would also like to thank Dr. Jia Zhou and Dr. Miki Nakayama for all of your help on my research, Danielle Nerko for your assistance in experiments and writing, Joe Magee for your humorous and smart talking, Pan Xu, Fang Xu and Si Luo for all the happiness with you and all the group members for everything I have learned in the past year.

Chapter 1. Introduction

The interfacial electronic properties of adsorbates on solid surfaces have been attracting growing attention because they provide a way to investigate the mechanism of interfacial heterogeneous catalysis and improve these catalysts' performance[1,2]. Through the interfacial interaction between adsorbates and substrate, the electronic properties of adsorbates and surfaces will be significantly influenced, including the electronic structure[3], charge state[4], interfacial charge transfer[4,5] and dipole moment[6,7]. This thesis focuses on the surface dipole and charge transfer at the interface of size-selected metal oxide and sulfide clusters on the Cu(111) surface and a Cu_2O/Cu(111) film to better understand their relationship with cluster-substrate interaction.

Interfacial charge transfer, usually a good descriptor of adsorbate-substrate interaction, plays an important role in the performance enhancement of heterogeneous catalysts[4] and organics-based electronic devices[6]. Electrons transferred from substrate to clusters can occupy the antibonding orbitals of adsorbed gas molecules on clusters, which can activate the gas molecules to induce bond cleavage[4]. Electron transfer at the organic-metal substrate interface in the light emitting diodes, can also contribute to the surface dipoles at the interface and induce substrate work function shift, which can improve the hole and electron injection efficiency[6]. Local electron affinity and electronegativity differences of species at interfaces are the driving forces of interfacial charge transfer. By comparing the adsorbate and substrate electron affinities, a rough estimation can be made on charge transfer direction and magnitude. Charge transfer will influence the surface dipole at the interface and thus induce a surface work function shift, which is easy to measure and accurate in showing the orientation and magnitude of charge transfer[8]. Figure 1.1 shows a schematic drawing of the relationship between substrate work function shift $\Delta\Phi$, surface dipole moment, $\mu_{surface}$, cluster dipole
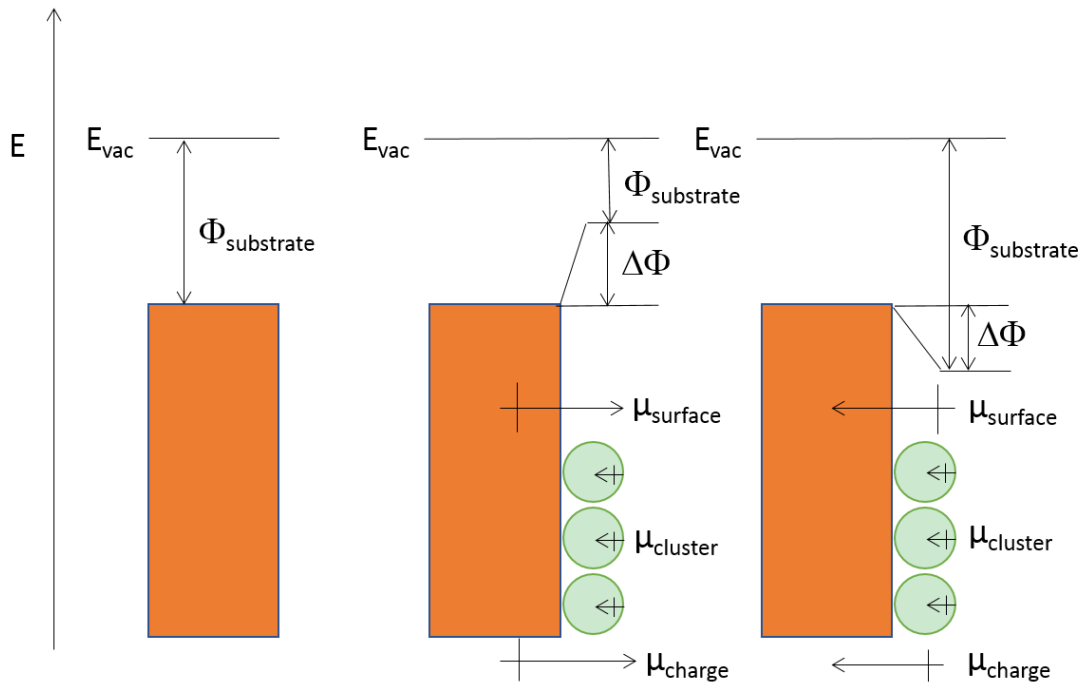
Figure 1.1: Schematic relationship between substrate work function shift $\Delta\Phi$, surface dipole moment $\mu_{surface}$, cluster dipole moment $\mu_{cluster}$ and dipole moment induced by interfacial charge transfer μ_{charge}.

moment, $\mu_{cluster}$ and dipole moment induced by interfacial charge transfer, μ_{charge}. The surface dipole is interpreted as a result of contributions from both deposited cluster dipole moment and charge transfer induced dipole moment. The orientation and magnitude of the surface dipole is directly proportional to the substrate work function shift, and μ_{charge} can be calculated by subtracting $\mu_{cluster}$ from $\mu_{surface}$, which provides information on interfacial charge transfer.

Metal particles dispersed on selected metal oxides have already been proved to be very active catalysts in chemical industry and environmental protection[9]. Of particular interest are metal oxide-supported Cu catalysts, which are found to be active towards several industrially important reactions. MgO(100) supported Cu nanoparticles are found to be active for the water gas shift (WGS) reaction, where Cu nanoparticles with low-coordinated corner and edge sites are associated with the water O-H bond cleavage[10]. ZnO(000$\bar{1}$) supported Cu nanoparticles exhibit high catalytic activity on CO_2 hydrogenation to produce methanol, where low-coordinated Cu sites on Cu nanoparticles can stabilize the key intermediate and lower the rate-limiting hydrogenation step barrier[11]. Besides the active sites in Cu nanoparticles, the metal oxide support has been shown to also take part in the catalytic activity enhancement. The metal oxide support can not only behave as a template for Cu nanoparticle dispersion, but also play a direct role in the generation of key intermediates during reactions[10]. In addition to metal oxide-supported Cu catalysts, Cu metals combined with molybdenum sulfide (MoS_2) films are found to enhance the hydrodesulfurization (HDS) reaction activity compared to pure MoS_2 films, where metal-metal interaction and hydrogen dissociation enhancement are thought to be responsible for the higher activity[12]. In order to be able to tune the catalyst activity, a better understanding of the

3

interaction at the metal oxide/sulfide and Cu interfaces is needed, including the electronic structures and possible interfacial charge transfer.

Besides the focus on conventional oxide supported catalysts, inverse model catalysts, have attracted considerable attention recently[13,14]. As opposed to conventional catalysts in which metal nanoparticles are usually supported on an oxide surface, inverse catalysts are composed of well-defined metal supports with metal oxides or sulfides deposited on them. The catalytic activity of some conventional catalysts can be enhanced when used as inverse model catalysts[15]. It was reported by Yan[15] that by growing Fe_2O_3 nanoclusters on a Au(111) single crystal surface which was initially inert for CO oxidation, an active catalyst was created which showed increasing activity for CO oxidation as the coverage of Fe_2O_3 nanoclusters got larger. However, when the coverage of Fe_2O_3 nanoclusters went above 0.5 ML, the activity started decreasing, demonstrating the Fe_2O_3/Au perimeter sites to be the active sites for CO oxidation. Gan[16] also proposed that the improved selectivity of the NiO_{1-x}/Cu(111) inverse catalyst for the WGS process was due to the suppression of undesired methanation during WGS process compared to a CuNi model system. The advantage of adopting inverse model catalysts is that it is possible to study interactions at metal oxide/support interface, which also exist in the traditional metal/oxide catalyst, as well as the interactions at defect sites of the oxide particle which only exist in inverse model catalysts. The oxide-metal interactions in inverse model catalysts, can influence the electronic states of oxide and metal support, which can result in new chemical properties and different catalytic performance[17]. Another advantage of inverse model catalysts is that some spectroscopy techniques, such as two photon photoemission spectroscopy and Auger electron spectroscopy can be readily applied since these

techniques require the support to be conductive while many oxide species are semi-conductors or insulators[18].

In order to investigate the cluster-substrate interaction, it is critical to have precise control over the size and composition of clusters on the substrate, since it is widely reported that nanoclusters with different sizes exhibit very different catalytic activities[19,20]. A unique approach which can easily deposit monodispersed clusters onto a substrate is using a size-selected cluster deposition apparatus. It can selectively deposit the desired clusters on a substrate by mass-selecting a single cluster from a full cluster distribution. The kinetic energy of the clusters can be tuned, which ensures clusters to achieve "soft-landing"[21] on the substrate with intact structure. Typically, the size-selected cluster deposition apparatus is composed of a cluster source, a quadrupole mass-selection filter and a UHV analysis chamber with differential pumping set-up all along the apparatus. In Chapter 2, the apparatus will be introduced in detail as well as two-photon photoemission spectroscopy (2PPE), Auger electron spectroscopy (AES) and temperature programmed desorption (TPD) techniques within the ultrahigh vacuum (UVH) analysis chamber. The experimental methods will be discussed at the end of the chapter.

A recent density functional theory (DFT) study has shown a strong correlation of WGS reaction activity with the interfacial electronic structure of stoichiometric metal oxide clusters deposited on Cu(111) surface[22]. The electronic structures are found to be significantly influenced by interfacial charge transfer through Bader charge analysis. In order to further investigate the interfacial electronic structures experimentally, stoichiometric metal oxide clusters (Mo_3O_9, W_3O_9 and Ti_3O_6) were selectively deposited on the Cu(111) surface and characterized by AES, 2PPE and TPD techniques. As a comparison to the stoichiometric clusters, more "reduced" clusters with lower

metal oxidation state (Mo_3O_6, W_3O_6) were also studied. Insight into the cluster size, was studied by comparing the results for the Ti_5O_{10} and Ti_3O_6 clusters. Besides the metal oxides, Mo_4S_6 clusters deposited on Cu(111) are also investigated in this work, which can provide information of interfacial charge transfer difference between metal oxides and sulfides. Lastly, we have also performed experiments to deposit Ti_3O_6 and Ti_5O_{10} clusters on the Cu_2O/Cu(111) film and investigate metal oxide cluster-substrate interactions. The Cu_2O film has been reported to exhibit different topological defects[23] from those of the Cu(111) and Cu_2O(111). These topological defects could improve catalytic activity compared to Cu(111) and we wanted to further investigate the cluster-Cu_2O/Cu(111) interaction using 2PPE spectroscopy.

In Chapter 3 of this thesis, detailed experimental results of interfacial charge transfer and surface dipoles will be discussed. AES spectra were used to monitor the cluster distribution on the substrate and estimate the local cluster coverage at different positions of the substrate. 2PPE spectra were used to derive the work function shift of the cluster deposited surface and showed a consistent increase of work function with increasing cluster coverage. The work function shift was further used to derive the surface dipole moment. In addition, since CO and water are highly involved in a lot of industrially important reactions[24,25], TPD of ^{13}CO and D_2O were taken, which probed the interaction of CO and D_2O with the metal oxide/Cu(111) systems and their binding energies to the cluster-metal surface.

Chapter 2. Experimental Section

In this chapter, vacuum and spectroscopic instrumentation which are involved in the experiments will be introduced. Experimental methods will also be presented. Section 2.1 will be a description of the size-selected cluster deposition apparatus. Section 2.2 will be an introduction to the UHV surface analysis chamber setup. Section 2.3 will mainly focus on the experimental methods.

2.1 Size-Selected Cluster Deposition Apparatus

Size-selected gas-phase nanocluster deposition is achieved in the apparatus shown in Figure 2.1. It is mainly composed of five parts which are a magnetron source, quadrupole ion guide, quadrupole mass filter, hexapole ion guide and quadrupole bender, in the order of nanocluster flow. Nanoclusters are produced in the magnetron source with typical pressure of $2{\sim}4{\times}10^{-3}$ Torr and transferred to the UHV surface analysis chamber whose typical pressure is $1{\times}10^{-9}$ Torr. In order to maintain the UHV environment in the surface analysis chamber without being affected by the relatively high pressure in the magnetron source, the differential pumping strategy is used here to let the pressure gradually drop from the magnetron source to the UHV analysis chamber with the assistance of six turbomolecular pumps.

Gas-phase nanoclusters are made in the magnetron source, where gas-phase atoms and clusters are produced by sputtering a metal target with Ar and small percentage of a reactive gas, such as oxygen to make metal oxide clusters. An aggregation gas, He, is added into the expansion chamber to cool and cause cluster formation. This type of magnetron source was developed by Haberland et al.[26] to produce metal cluster ions but has proved to be effective in the production of compound clusters as well[27]. The source used here was a commercial source manufactured by Oxford Applied Research (NC200U). The metal target is fixed on a rare earth magnet with a cap holder. Sputtering gas (Argon gas) and reactive gas (O_2/Ar mixture) flow into the magnetron source regulated by a mass flow controller (MKS). Once a high voltage is applied between the metal target and cover, a glow discharge is produced. The argon plasma is confined above the target and Ar^+ is driven towards the target to sputter it. Sputtered metal clusters are oxidized by O_2 and collide with the He aggregation gas to form a series of metal oxide nanoclusters. To control the composition

8
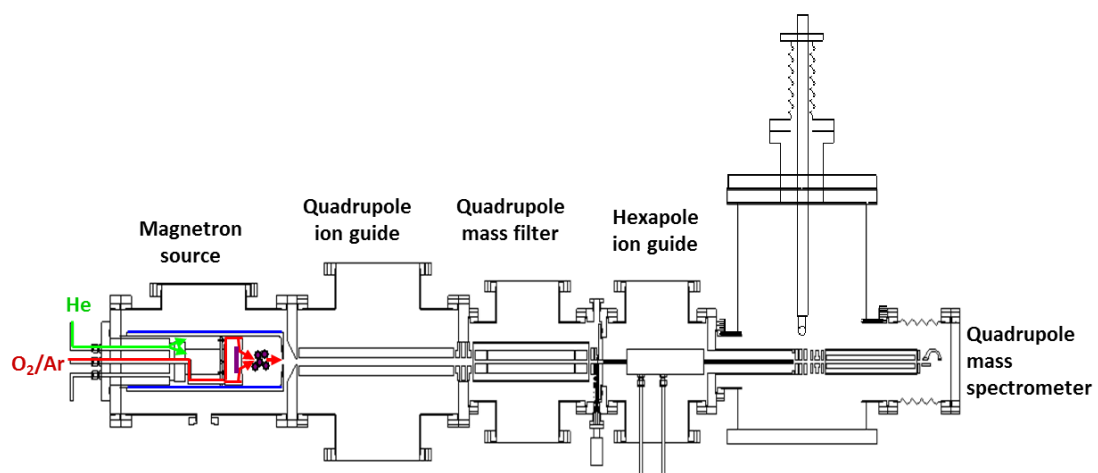
Figure 2.1: Schematic side-view of the mass-selection deposition apparatus.

and intensity of produced clusters, a lot of parameters can be adjusted such as the sputtering gas pressure, aggregation gas pressure, sputtering voltage and aggregation volume. Figure 2.2 is a typical nanocluster distribution spectrum of Mo_xO_y clusters.

The mass filter to select a specific cluster ion is a quadrupole system composed of two pairs of rods, which are evenly spaced around the designed path of the nanocluster flow. While opposite rods are electrically connected, rods next to each other are electrically isolated. Direct current (DC) and radio frequency (RF) voltages are applied to the rods so as to form a hyperbolic electric field between them. The stability of the nanocluster ions going through the quadrupole can be controlled by tuning the amplitude of DC and RF voltages and the RF frequency. Two dimensionless parameters a and q, are used to describe the motion of the ions through the mass filter:

$$a = \frac{4eU}{m\omega^2 r_0^2} \tag{2.1}$$

$$q = \frac{2eV}{m\omega^2 r_0^2} \tag{2.2}$$

where U is the DC voltage, V is the RF amplitude, m is the nanocluster mass, ω is the RF angular frequency, r_0 is the distance from the center of nanocluster flow to the edge of rods. By replacing $\omega t/2$ by ξ, the stability of the ions going through the quadrupole can be described by the following equation[28] which is a standard form of Mathieu equation:

$$\frac{d^2u}{d\xi^2} + (a - 2q\cos(2\xi))u = 0 \tag{2.3}$$

10
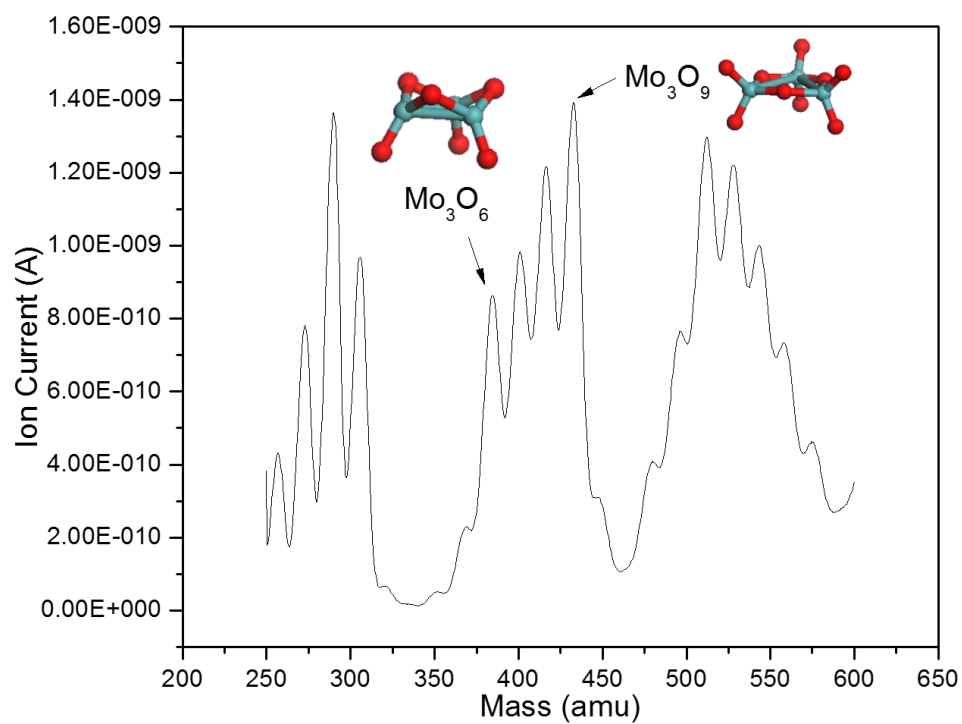
Figure 2.2: Mass distribution spectrum of Mo_xO_y clusters and the DFT gas phase structures of Mo_3O_6 and Mo_3O_9 clusters. The Mo_3O_9 DFT structure is from reference [22].

where u is the position of nanoclusters. To get stable solutions for this equation, a and q must be a combination with appropriate values, which provides a way to control the ions going through the quadrupole systems. By using a power supply whose design was proposed by R. M. Jones et al.[29], the quadrupole ion guide is set to be in RF-only mode, which applies 180 degree out of phase RF potentials with a frequency of around 600 kHz to the rods. In this mode, the quadrupole ion guide will act as a high pass filter. However, we can change the DC voltage and RF potential in the quadrupole mass filter. Thus, we can get a nanocluster mass distribution spectrum or select only one type of nanocluster with a certain mass to be transmitted.

Once certain ionic nanoclusters with specific mass are selected after going through the quadrupole mass filter, the hexapole ion guide will keep transporting them into the surface analysis chamber in order to deposit them onto the Cu(111) single crystal surface. However, neutral nanoclusters cannot be blocked by the quadrupole mass filter and they will also be transmitted into the chamber with ionic species. These neutral species have unknown sizes and chemical compositions so that it is necessary to separate them from ionic species. Thus, a quadrupole bender is used after the hexapole ion guide to deflect the ionic nanoclusters by 90 degrees, while the neutral ones will keep going straight. This is shown in Figure 2.3. A picoammeter is connected to the Cu crystal, which can record the current of ionic nanoclusters landing on the Cu crystal. The current will then be transformed into the number of nanoclusters by the deposition software. It is also crucial to achieve "soft landing"[21] of the nanoclusters so that their structures will stay intact when landing on the Cu(111) surface. Thus, a bias is applied to the crystal, in order to decelerate nanoclusters so that the kinetic energy for most of the clusters will be below 2 eV, which is typical soft landing kinetic energy[30].
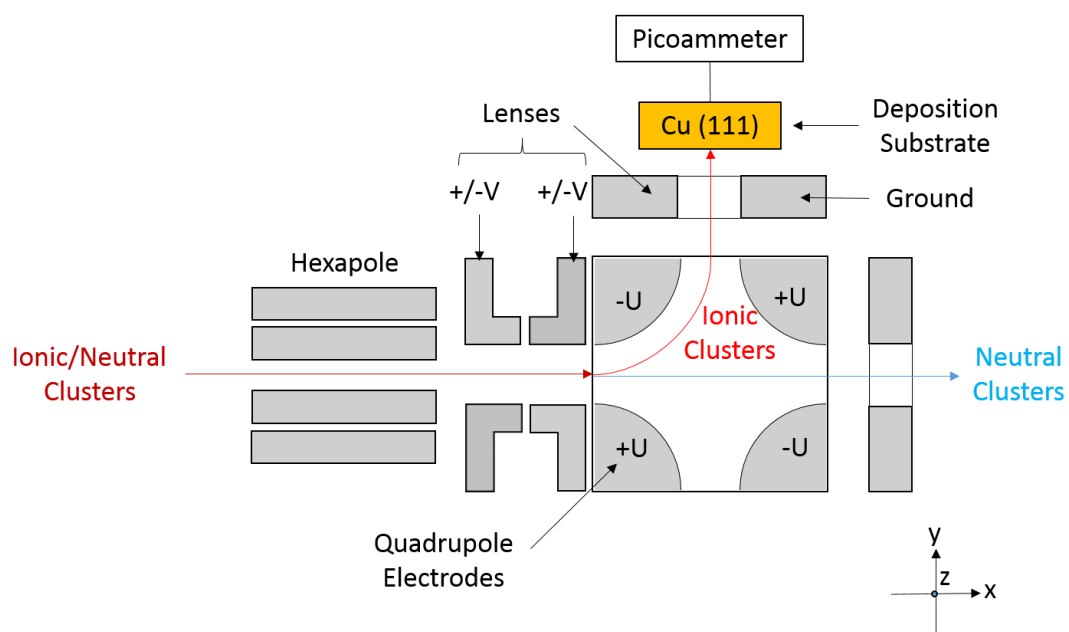
Figure 2.3: Schematic of the nanocluster flow path from hexapole to quadrupole bender and Cu(111) surface.

2.2 UHV Surface Analysis Chamber

A schematic of the upper and lower levels of the UHV surface analysis chamber are shown in Figure 2.4. The chamber is pumped by two turbomolecular pumps simultaneously and the typical pressure in the chamber is $4 \sim 9 \times 10^{-10}$ Torr. The chamber is equipped with vacuum and spectroscopic instrumentation for Cu(111) crystal surface cleaning, temperature programmed desorption (TPD), Auger electron spectroscopy (AES) and two-photon photoemission spectroscopy (2PPE). The Cu(111) single crystal and involved characterization techniques will be described in this section.

2.2.1 Cu(111) Single Crystal Substrate

The Cu(111) single crystal (Princeton Scientific) substrate has a diameter of 11 mm and a thickness of 2 mm. It is fixed on a tantalum mount with a piece gold foil between them, which is used for improving the heat conductivity. The mount has two tantalum wires, which are connected to a copper vacuum feed-through at the bottom of a stainless steel hollow tube. The tube can be used as a reservoir for liquid nitrogen (LN$_2$). An XYZ translator and a rotation stage are mounted at the top of the tube, with which precise translation and rotation of the Cu(111) substrate can be achieved. A K-type thermocouple is mounted to the side of the Cu crystal in a small machined hole. By applying LN$_2$ cooling and resistive heating, the temperature of the Cu crystal can be controlled in the range of $105 \sim 800$ K. The Cu(111) surface was cleaned by Ar$^+$ sputtering and annealing after sputtering at 700 K. After a routine cleaning procedure of two cycles of sputtering and annealing, no impurity from previous cluster deposition was detected by AES.

(a)
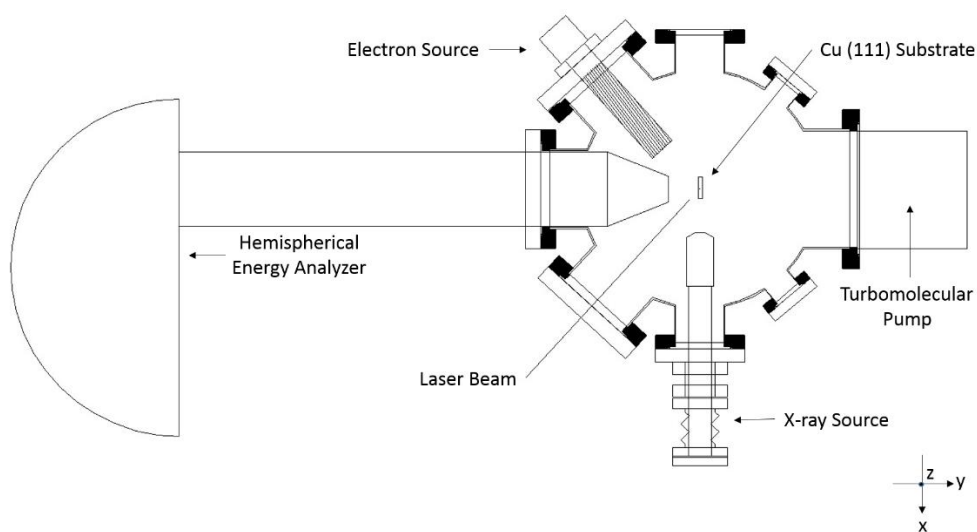
(b)
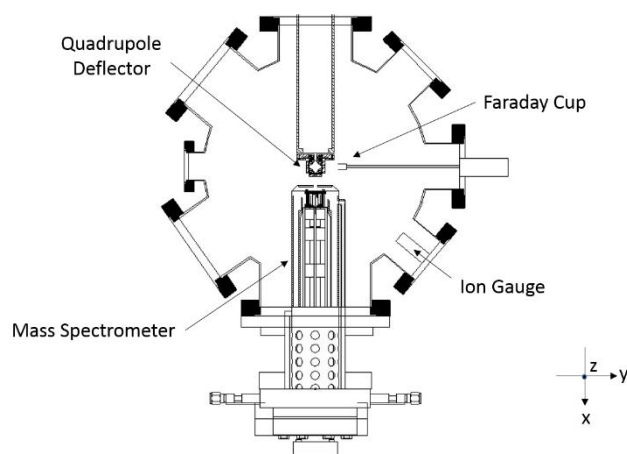
Figure 2.4: Schematic of UHV surface analysis chamber at (a) upper level and (b) lower level.

2.2.2 Temperature Programmed Desorption

Temperature programmed desorption (TPD) is used for studying the desorption rate and binding energy of adsorbates pre-dosed on sample surface. In a typical TPD experiment, target molecular species are dosed onto the sample surface at a relatively low temperature. After that, the sample is heated up linearly and the counts of target molecular species per unit time, will be monitored as a function of temperature. To estimate the binding energy E_{ad} of adsorbates, the Redhead model[31] is commonly used:

$$E_{ad} / RT_P = \ln(\nu T_P / \beta) - \ln(E_{ad} / RT_P) \qquad (2.4)$$

where R is the gas constant, T_P is the temperature of maximum desorption rate, ν is the pre-factor and β is the heating rate. The pre-factor is usually treated as 10^{13} s^{-1} and reasonable results can be found when ν/β lies in the range of $10^8 \sim 10^{13}$ K^{-1}.

In our TPD experiments, once the crystal is cooled to a desired temperature at which the molecules would stick to the surface, the UHV surface analysis chamber is then backfilled with target adsorbate molecules to certain pressure using a leak valve. After dosing the adsorbate molecules for a measured period, the valve will be closed and the crystal will be heated up in front of a quadrupole mass spectrometer (Hiden) to monitor the adsorbate desorption. The molecules are ionized and selectively detected by the quadrupole mass spectrometer with different combinations of DC and RF voltages. A process control unit (Eurotherm) is used to linearly ramp up the crystal temperature at a typical rate of 1.5 K/s.

2.2.3 Two-Photon Photoemission Spectroscopy

Two-photon photoemission spectroscopy (2PPE) is quite powerful and sensitive in detecting valence electronic states and work function shifts. Figure 2.5 shows two

Figure 2.5: Schematic energy diagram of typical 2PPE processes with (a) an unoccupied intermediate state or (b) a virtual intermediate state.

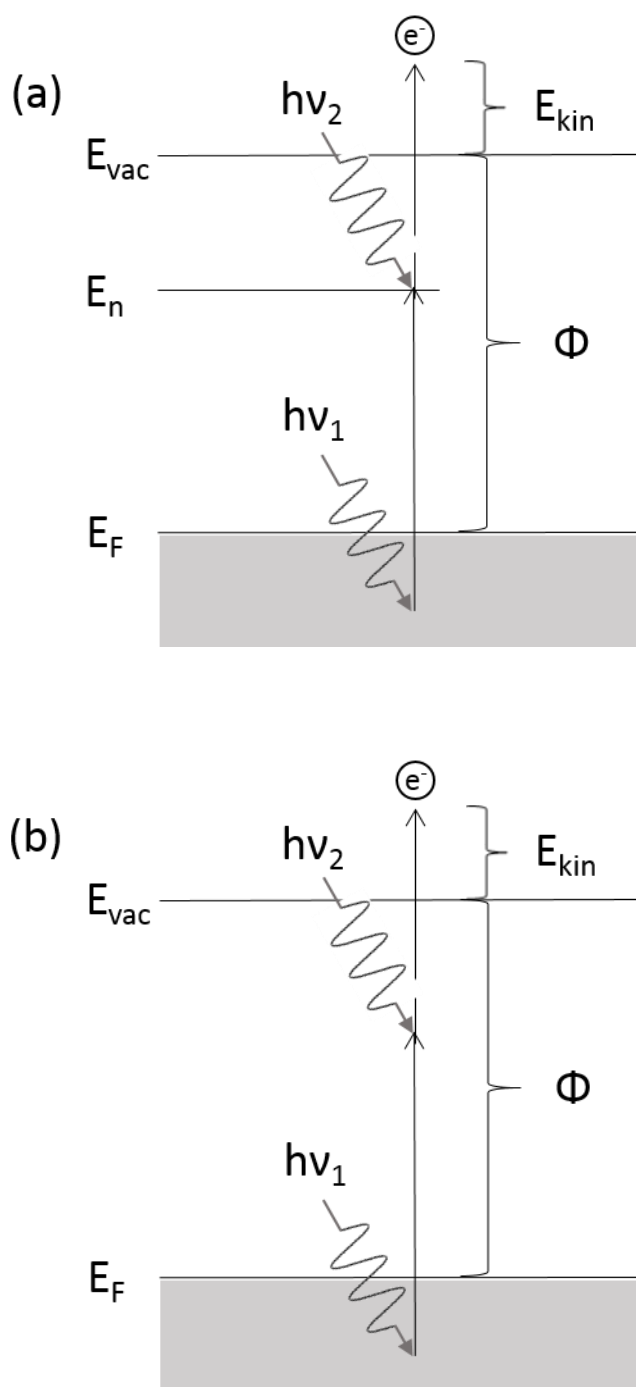types of 2PPE processes. In process (a), the first photon excites an electron from an occupied state below Fermi level to an unoccupied intermediate state. Then, the second photon can further excite the electron to a final state above vacuum level. These two photons do not need to have different wavelengths. The other 2PPE process, shown in Figure 2.5b is quite similar as the first one, but now the intermediate state is actually a virtual state, which is not a real electronic state. Thus, the 2PPE process here has to be a coherent two-photon process, where the interval between two photons has to be within a range[32], which is typically below 20fs[33]. Based on the mechanism differences of these two processes, one can easily tell whether the intermediate state is real or not by observing the relationship between the final kinetic energy of the excited electron and the energy of the first photon. If the kinetic energy of the electron varies with both the energy of the two photons, then the intermediate state is a virtual state. If the kinetic energy of the electron just depends on the energy of the second photon, the intermediate state is a real unoccupied electronic state.

In our 2PPE experiments, a Ti:Sapphire oscillator (Spectra-Physics Tsunami) is used as the laser source. It is pumped by a solid-state $Nd:YVO_4$ laser with 5 W continuous wave power at 532 nm (Spectra-Physics Millennia V). The pulses generated by the Ti:Sapphire oscillator are around 100 fs, which can be tuned in the wavelength range of 720 ~ 850 nm. Normally, pulses are tuned up around 830 nm which corresponds to photon energy of 1.49 eV. However, this photon energy is not enough to excite electrons from a typical crystal surface with the work function in a common range (Cu(111), 4.9 eV[34,35]). Thus, a nonlinear optical crystal is applied to combine the photons to get new ones with doubled and tripled frequency via second (SHG) and third harmonic generation (THG), respectively. The THG pulses are used for our 2PPE experiments and have a photon energy of 4.48 eV. The SHG and THG wavelengths are

produced is a time-plate harmonic generator (Photop TP-2000B), which can control the polarization and beam path length of the fundamental beam and the second harmonic wave so that they can efficiently combine to form third harmonic generation. The schematic laser beam path is shown in Figure 2.6.

2.2.4 Auger Electron Spectroscopy

Auger Electron Spectroscopy (AES) is also a very important spectroscopic technique in surface science, as it can selectively detect atoms from several atomic layers at the top of the surface (5 ~ 20 Å)[36]. In a typical AES process, a core electron is removed by a high energy photon or electron. As a result, a hole is left which will be filled by an outer shell electron. Because the hole is in a lower energy level, a certain amount of energy will be released which can excite another electron in the outer shell into the continuum. This is called the Auger process and the kinetic energy spectrum of ejected electrons is measured by an electron spectrometer. Because different elements have characteristic kinetic energy spectra, Auger electron spectrometry can be used to identify various elements and their surface concentration near the surface.

In our experiments, we integrate the areas under O KLL peak to calculate the relative amount of clusters at different positions. An electron gun (EQ 22/35, Specs) is used as the electron beam source, which operates at a voltage of 5 kV. It is positioned 45° with respect to the Cu(111) surface, while the hemispherical analyzer (Phoibos 100, Specs) is located normal towards the crystal surface. The crystal is electrically grounded so that it will not be charged by the electron beam.
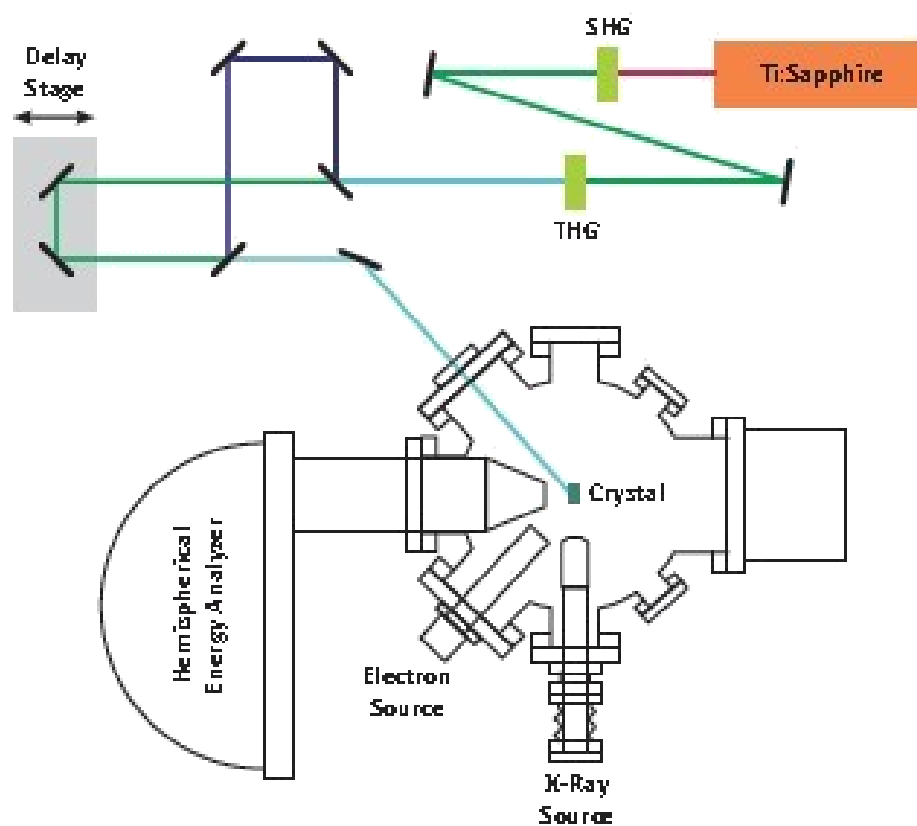
Figure 2.6: Schematic laser beam path from Ti:Sapphire oscillator to the main chambers.

2.3 Experimental Methods

The surface analysis chamber is pumped by two turbomolecular pumps simultaneously so that the normal chamber pressure can be kept in the range of $4 \sim 9 \times 10^{-10}$ Torr. It is also equipped with crystal cleaning equipment, temperature control device and spectroscopic instrumentation, which can be used for daily experiments and maintenance. The Cu(111) crystal was cleaned before deposition and spectroscopic probing, with two cycles of Ar^+ ion sputtering for 30 min and annealing at 700 K for 20 min after each sputtering. In order to make the Cu_2O film on the Cu(111) substrate, a previously established method was used[37]. The Cu(111) substrate was annealed at 650 K for 20 min with background O_2 pressure of 5×10^{-7} Torr. After that, the crystal was cooled in the O_2 background atmosphere until 400 K to prevent the Cu_2O film from decomposing.

Once the crystal surface was clean and ready for deposition, clusters were size-selected and deposited on the crystal surface. Briefly, metal oxide clusters (Mo_xO_y, Ti_xO_y, W_xO_y) were produced by sputtering metal targets with an Ar/O_2 mixture in the magnetron source. Clusters would then be transported through the quadrupole ion guide and mass-selected in the quadrupole mass filter. After being guided by the hexapole ion guide, selected clusters were deflected by the quadrupole bender by 90^0 so as to be separated from the neutral species and decelerated to achieve soft landing. Before being deposited on the clean crystal surface, clusters would be deposited on the Faraday cup first, whose intensity would be selectively monitored and enhanced by tuning the relative composition and pressure of Ar/O_2 mixture, He gas pressure, aggregation compartment volume, magnetron sputtering voltage, quadrupole an hexapole ion guide voltage and the voltage of lenses and benders. Once the intensity of selected clusters

was optimized, we would begin depositing clusters onto the crystal surface, while controlling and monitoring the deposition parameters and ion current in a LabView program. By integrating the ion current on the crystal surface, the total number of deposited clusters can be calculated.

AES spectra were used to qualitatively and quantitatively analyze the cluster deposition. Since metal peaks were not strong enough to provide accurate quantitative information, the oxygen peak (KLL, 513 eV) was used to map the cluster distribution instead. "Line scans" were used to collect the Auger spectra in both horizontal (x-axis) and vertical (z-axis) directions, with a spacing of 0.50 mm. The deposition area containing 90% of the clusters had a radius of around 3 mm in both horizontal and vertical directions. Since the Auger beam size was no more than 0.25 mm, which was much smaller than our total deposition area, it was reasonable and precise to plot the cluster distribution with the AES spectra at different spots separated by a spacing of 0.50 mm. The integration of the oxygen peak at each position was taken, which was further fitted (Gaussian fit) to generate the deposition distribution functions. Thus, the average cluster coverage (in the unit of monolayer) could be calculated by dividing the total area of clusters in a crystal area at a selected position by the crystal area. The total area of clusters was estimated by multiplying the total number of clusters by the area per cluster, which was derived from the density functional theory (DFT) calculation.

The work function shift was measured using the two-photon photoemission spectroscopy (2PPE), and a brief description is given here. Initially, a Ti:Sapphire oscillator (Spectra-Physics Tsunami) was used to generate laser beams at a wavelength of 830 nm. Photons in the fundamental laser beams were combined to produce second (SHG) and third harmonic generations (THG), while THG with photon energy of 4.48 eV were used in our 2PPE experiments. An optic lens was used to focus the THG beams

on the crystal surface, whose focal length was 38 cm. Thus, the size of the focused beam was estimated to be no more than 0.25 mm, which enabled a same "line scan" method as that of AES to be applied on the crystal surface, but with a spacing of 0.25 mm. In order to get a better intensity of electrons with low energy, a -4 V bias was applied to the crystal. Thus, the low-energy secondary electron cutoff could be analyzed more precisely, which represented the work function with the contribution of the bias. By analyzing the 2PPE spectra at different positions, the work function shift was plotted and fitted by the Gaussian fit. It was further correlated with the AES data to plot the figures of the relationship between work function shift and local cluster coverage.

In this thesis, the DFT calculations on structures of $Mo_3O_6/Cu(111)$, $W_3O_6/Cu(111)$ and $Ti_5O_{10}/Cu(111)$ and radii of all the systems were performed by Yixiong Yang. The rest of the DFT results will appear in a paper to be published.

Chapter 3. Results and Discussion

3.1 Cluster Distribution and 2PPE Spectra

Figure 3.1a shows a typical AES spectrum of Mo_3O_9 clusters, deposited on Cu(111) surface. Because the normalized Mo MNN peak sensitivity factor (217 eV, 0.553) was smaller than that of O KLL peak (513 eV, 0.788)[38] and the concentration of O atoms was three times greater than Mo atoms, the O KLL peak integration was plotted in terms of distances from the center of cluster deposition area along the horizontal (x-axis) and vertical (z-axis) directions, which represented the cluster line distribution from the center to the edges of deposition area. The cluster line distribution could be described by the a Gaussian function along both the horizontal and vertical directions, from which the two-dimensional Gaussian function could be derived to plot the Mo_3O_9 cluster distribution on the Cu(111) surface, as shown in Figure 3.1b.

Similar line scan methods have also been used for 2PPE spectra. Figure 3.2 shows the 2PPE spectra for the Mo_3O_9/Cu(111) surface with different local coverage. These spectra were taken using the third harmonic with photon energy of 4.48 eV. Work function corresponds to the low-energy cutoff position of the secondary electron peak and the small band right after the secondary electron peak is the Cu 3d band. The Cu(111) first image state (IS), which lies 0.8 eV below vacuum level (E_{vac})[39], corresponds to a final state energy of 8.53 eV in the spectra while the Cu(111) surface state (SS), which lies 0.4 eV below Fermi level (E_F)[39,40], corresponds to a final state energy of 8.56 eV. The 2PPE spectrum with no Mo_3O_9 coverage represents the bare Cu(111) surface spectrum and it shows a work function of 4.85 eV. The latter is consistent with previous reported Cu(111) work function values which are around 4.9 eV[34,35]. As the local Mo_3O_9 cluster coverage increases, the work function keeps shifting
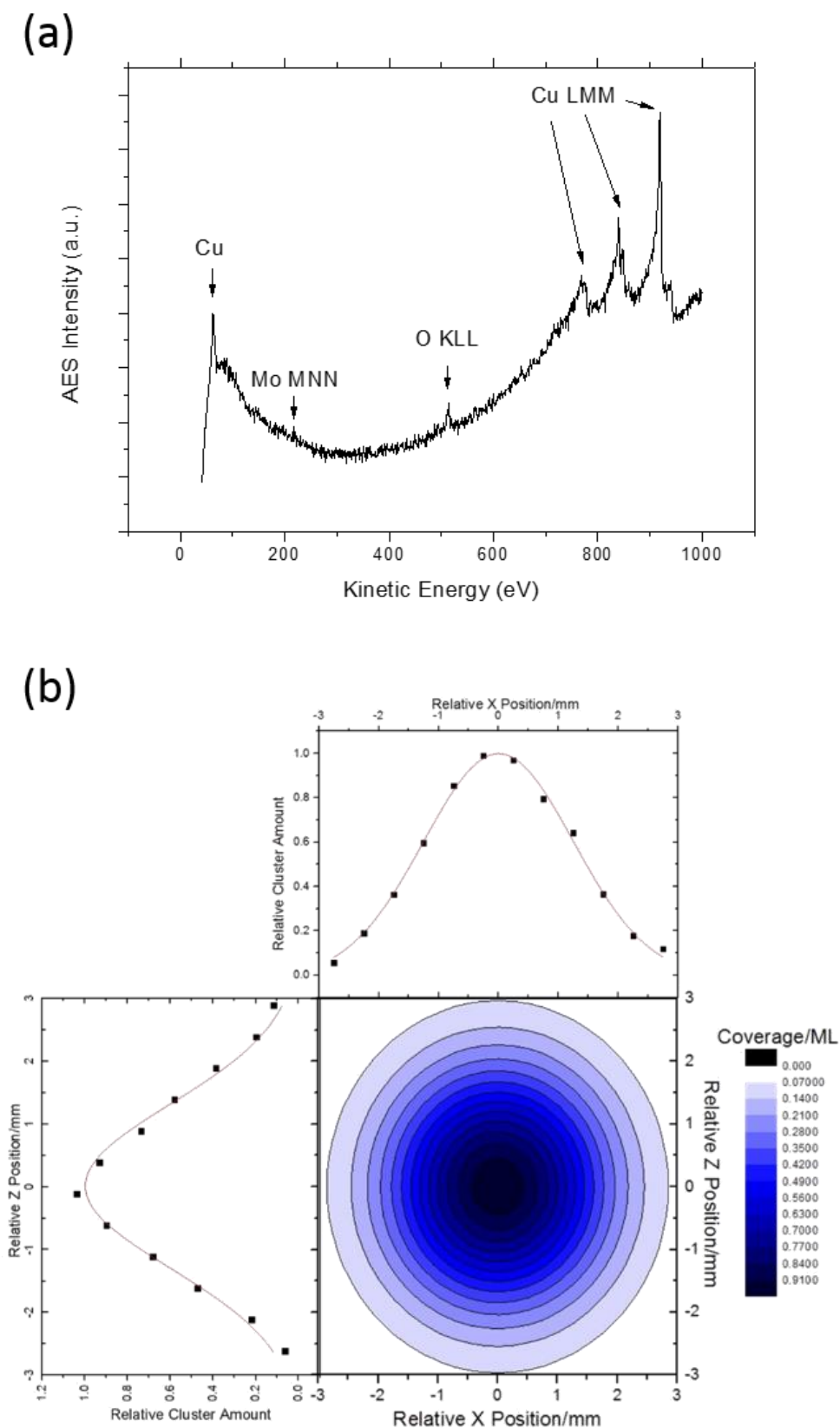
Figure 3.1: (a) AES full scan of Mo_3O_9 deposited on Cu(111); (b) Gaussian fit of Mo_3O_9 nanocluster distribution along horizontal (Top) and vertical (Left) direction and two-dimensional Mo_3O_9 nanocluster coverage distribution (Lower Right).
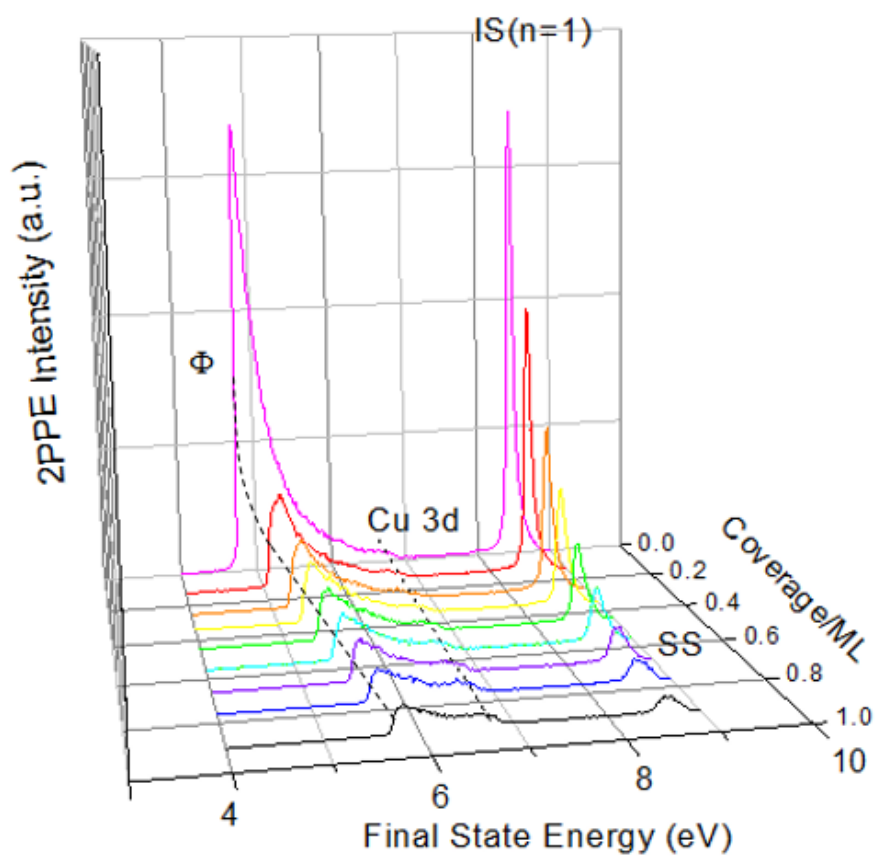
Figure 3.2: Three-dimensional 2PPE spectra of $Mo_3O_9/Cu(111)$ with different local cluster coverage.

to higher values, with a larger slope in the lower coverage regime and a smaller slope at higher coverage area. The IS and SS states cannot be fully resolved in our 2PPE spectra, which results in an asymmetric peak around 8.48 eV in the bare Cu(111) spectrum. As the local Mo_3O_9 cluster coverage increases, the photoemission from the IS keeps declining until being fully quenched, while the photoemission from SS also shows weaker intensity.

Using the two-dimensional Gaussian function of the Mo_3O_9 cluster distribution on the Cu(111) surface and the measured total number of Mo_3O_9 clusters deposited, the number N of deposited clusters within a certain substrate area S can be easily derived. Thus, the cluster density n_a can be calculated as:

$$n_a = N / S \qquad (3.1)$$

and the cluster coverage θ (monolayer, ML) can be defined as:

$$\theta = n_a \times A \qquad (3.2)$$

where A is the cross sectional area of the cluster. To estimate A, the cross section of the cluster was assumed to be circular or oval and the cluster radius was derived from density functional theory (DFT) calculations. The DFT structure and interfacial bonding of deposited Mo_3O_9 clusters on Cu(111) is shown in Figure 3.3a. The Mo_3O_9 cluster bonds with the Cu(111) surface through the three O atoms at the top sites of Cu(111). The radius of the deposited Mo_3O_9 cluster was calculated to be 4.52 Å. The kinetic energy of Mo_3O_9 clusters was below 2 eV, when deposited on the Cu(111) surface. This assures that the kinetic energy per atom is below 0.2 eV, which is a typical "soft landing" condition. Thus, the clusters and the Cu(111) surface itself will stay intact during deposition.
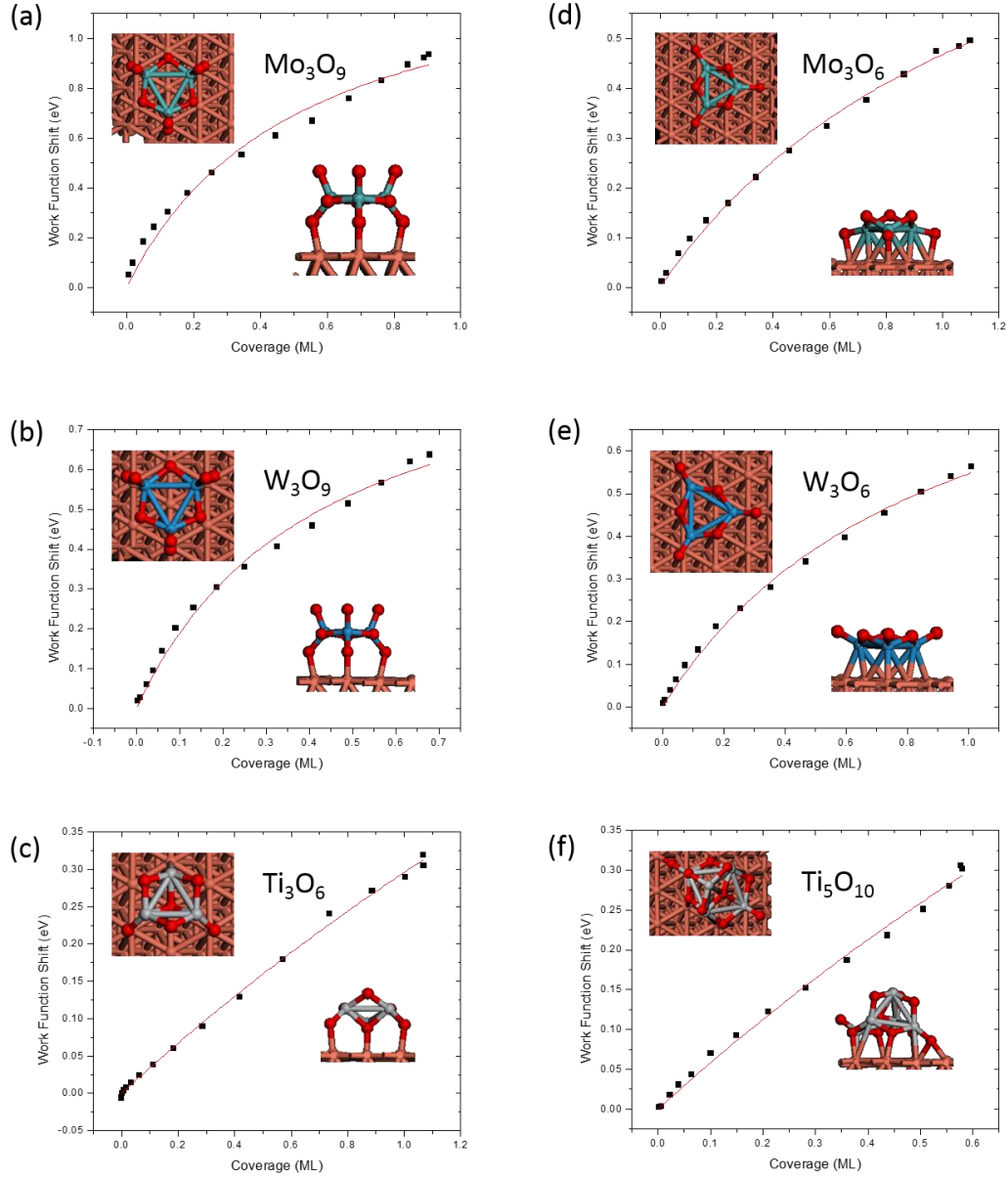
Figure 3.3: Work function shift of (a) Mo_3O_9 (b) W_3O_9 (c) Ti_3O_6 (d) Mo_3O_6 (e) W_3O_6 (f) Ti_5O_{10} clusters deposited on Cu(111) surface in terms of local cluster coverage. The solid lines are fitting curves based on Topping model. The two DFT structures beside the fitting curve are the corresponding top view and side view of the optimized cluster configuration on Cu(111) surface (Brown: Cu; green: Mo; blue: W; gray: Ti; red: O). The DFT Structures in (a), (b) and (c) are from reference [22] and the DFT structures in (d), (e) and (f) are calculated by Yixiong Yang.

Besides experiments on $Mo_3O_9/Cu(111)$, similar AES and 2PPE experiments were also carried out on W_3O_9, Ti_3O_6, Mo_3O_6, W_3O_6, Ti_5O_{10} and Mo_4S_6 clusters deposited on $Cu(111)$ and Ti_3O_6 and Ti_5O_{10} clusters deposited on a $Cu_2O/Cu(111)$ film. In each case, their cluster distributions could be fitted to a two-dimensional Gaussian function and the work function shifts to higher values as the local cluster coverage increases. The optimized DFT adsorption structures are shown in Figure 3.3 and corresponding radii are listed in Table 3.1.

Table 3.1: Calculated radii, surface dipole moment μ, cluster Bader charge, gas phase electron affinity and polarizability of metal oxide clusters deposited on Cu(111) surface. As for dipole moments, the "-" sign means the direction of the dipole is from clusters to the Cu(111) surface.

Cluster	Mo_3O_9	W_3O_9	Ti_3O_6	Mo_3O_6	W_3O_6	Ti_5O_{10}
Radius (Å)	4.52	4.52	4.10	4.98	4.98	5.40/3.37
μ (D)	-4.62	-4.00	-0.49	-1.71	-2.39	-0.91
Bader Charge (e)	-1.37 [22]	-1.37 [22]	-0.33 [22]	---	---	---
Electron Affinity (eV)	4.0 [41]	4.2 [41]	3.15 [42]	2.98 [43]	2.95 [43]	4.13 [42]
Polarizability ($Å^3$)	$1.39×10^3$	$1.70×10^3$	$92.9×10^3$	$7.38×10^2$	$1.07×10^3$	$1.92×10^2$

3.2 Work Function Shift, Surface Dipole and Topping Model

The work function shifts, $\Delta\Phi$, of the previously described cluster/Cu(111) systems, are plotted in terms of local cluster coverage in Figure 3.3. For all the systems here, the work function shifts to higher values as the local cluster coverage increases. However, the magnitude of work function shift is different, and is dependent on the specific cluster. To analyze the dipole moment and polarization of these systems, the Topping model[44] is used which is shown as:

$$\Delta\Phi = \frac{en_a\mu}{\varepsilon_0}(1+\frac{9\alpha}{4\pi}\delta n_a^{3/2})^{-1} \qquad (3.3)$$

where e is the electron charge, μ is the surface dipole moment, ε_0 is the vacuum permittivity, α is the cluster polarizability and δ is the cluster mobility parameter. The term outside of the parentheses, represents the surface dipole moment contribution towards the change of work function, while the term in the parentheses describes the cluster polarization effect on work function shift. The polarization effect results from the dipole-dipole interaction, which strongly decreases the work function shift, when the cluster coverage becomes higher and the surface dipoles are much denser. For randomly distributed dipoles on the surface, which is appropriate under our experiment conditions, the cluster mobility parameter δ can be described by the lattice gas model[45]:

$$\delta = \theta^{-0.5} \qquad (3.4)$$

Based on equations (3.2) and (3.4), by substituting cluster density n_a and cluster mobility parameter δ in equation (3.3), equation (3.3) can be reorganized as:

$$\Delta\Phi = \frac{e\theta\mu}{A\varepsilon_0}(1+\frac{9\alpha}{4\pi A^{3/2}}\theta)^{-1} \qquad (3.5)$$

As shown in Figure 3.3, the solid lines represent the fits of the experimental work function shifts to equation (3.5). The surface dipole moment, μ, and cluster

polarizability, α, of all the cluster/Cu(111) systems are calculated and they are listed in Table 3.1. The surface dipole includes contributions from both the interfacial charge transfer and the permanent dipole moment of the deposited clusters. The latter can be neglected if the clusters are highly symmetrical along surface normal. In this case, the calculated surface dipole can just be treated as the dipole induced by interfacial charge transfer between the Cu(111) surface and the oxide clusters.

3.3 2PPE, DFT and TPD Study on Mo_xO_y, W_xO_y and Ti_xO_y Clusters Deposited on Cu(111) Surface

As described in Section 3.2, the DFT calculation on Mo_3O_9/Cu(111) shows that the Mo_3O_9 cluster is highly symmetrical with oxygen atoms evenly distributed above and below the Mo-atom plane, and bonds with the Cu(111) surface through the three terminal oxygen atoms at the top sites of Cu(111). Based on the highly symmetrical structure, it is reasonable to neglect the influence of the Mo_3O_9 cluster on the surface dipole moment. Thus, the resulted surface dipole moment, which is calculated to be -4.62 D and points from the Mo_3O_9 cluster to the Cu (111) surface, is attributed to the interfacial charge transfer. The calculated dipole moment shows that electrons are transferred from Cu (111) surface to the Mo_3O_9 clusters, which is consistent with the DFT calculated Bader charge transfer value of 1.37 e within the Mo_3O_9 Bader volume[22].

W_3O_9/Cu(111) has a very similar DFT structure as that of Mo_3O_9/Cu(111). The W_3O_9 cluster also bonds with Cu(111) surface through the three terminal O atoms at the top sites of Cu(111). In addition, Mo_3O_9 and W_3O_9 clusters were reported to have similar electron affinities, which were 4.0 eV and 4.2 eV, respectively[41]. Thus, a similar surface dipole moment as that of Mo_3O_9/Cu(111) is expected for W_3O_9/Cu(111). This is proved by calculation which shows a surface dipole moment of -4.00 D for W_3O_9/Cu(111). Electrons are also transferred from Cu(111) surface to the clusters, which is also expected by a Bader charge transfer value of 1.37 e within the W_3O_9 Bader volume[22].

However, different from Mo_3O_9/Cu(111) and W_3O_9/Cu(111), the DFT structure of Ti_3O_6/Cu(111) shows that oxygen atoms are not evenly distributed and the Ti_3O_6 cluster is bonded with the Cu(111) surface through both two terminal oxygen atoms,

one triple-bridge oxygen atom at the center and three titanium atoms. The reported electron affinity of 3.15 eV is also much smaller[42]. Thus, a weaker interfacial charge transfer is expected for Ti_3O_6/Cu(111). In Figure 3.3c, a distinct feature is observed, in which the work function shifts almost linearly with the increase of the Ti_3O_6 cluster coverage and the work function shift is smaller than that of Mo_3O_9/Cu(111) and W_3O_9/Cu(111) at the same cluster coverage. Surface dipole calculation agrees with previous expectation, which shows a significantly smaller surface dipole moment of -0.49 D. It correlates with a relatively small Bader charge value of -0.33 e^{22}, although the cluster dipole moment resulting from less symmetrical structure might also contribute to the lowering the overall surface dipole.

In order to further study the influence of metal cluster oxidation state on interfacial charge transfer, Mo_3O_6/Cu(111) and W_3O_6/Cu(111) are probed using 2PPE spectroscopy, which has a smaller metal oxidation state of +4, compared with +6 of stoichiometric clusters. Their surface dipole moments are calculated to be -1.71 D and -2.39 D, respectively. Their surface dipole moments are both much smaller, compared with the stoichiometric metal oxide clusters, Mo_3O_9/Cu(111) and W_3O_9/Cu(111). This indicates a smaller charge transfer from Cu(111) surface to the metal oxide clusters, compared with stoichiometric metal oxide systems. This can be rationalized by the smaller electron affinities, which are 2.98 eV for Mo_3O_6 and 2.95 eV for W_3O_6[43]. However, even with the a similar electron affinity of 3.15 eV[42], Ti_3O_6/Cu(111) shows a drastically smaller surface dipole moment of -0.49 D. A close look at the DFT structures of Ti_3O_6/Cu(111), Mo_3O_6/Cu(111) and W_3O_6/Cu(111) shows that these metal oxide clusters have very different structures. Ti_3O_6 and Mo_3O_6 bind on the Cu(111) surface with terminal oxygen atoms while W_3O_6 is bonded with Cu(111) though purely metal atoms. In addition, different from Ti_3O_6 and Mo_3O_6 which have the same number

of oxygen atoms above and below the cluster plane, all the oxygen atoms in W_3O_6 are above the cluster plane, which should induce a relatively larger cluster dipole moment. These two aspects might contribute together to the observed surface dipole moment difference among $Ti_3O_6/Cu(111)$, $Mo_3O_6/Cu(111)$ and $W_3O_6/Cu(111)$.

Lastly, $Ti_5O_{10}/Cu(111)$ is investigated to compare with $Ti_3O_6/Cu(111)$, in order to provide information on the influence of cluster size on interfacial charge transfer. As shown in Figure 3.3, both of them show linear shifts in $\Delta\Phi$ as the cluster coverage increases, which is different from $Mo_xO_y/Cu(111)$ and $W_xO_y/Cu(111)$. Since the electron affinity of Ti_5O_{10} is 4.13 eV, which is significantly larger than that of Ti_3O_6 (3.15 eV)[42], the interfacial charge transfer is expected to be stronger in $Ti_5O_{10}/Cu(111)$ than $Ti_3O_6/Cu(111)$. This is consistent with the derived surface dipole moment of -0.91 D for $Ti_5O_{10}/Cu(111)$, which is significantly larger than that of $Ti_3O_6/Cu(111)$ (-0.49 D). The larger cluster size and more available Ti^{4+} cations to accommodate the transferred electrons might be the reason for the larger surface dipole.

In addition to the 2PPE data described above, TPD experiments for ^{13}CO and D_2O were also performed on these systems. The ^{13}CO TPD spectra of clean Cu(111) surface and metal oxide clusters (Mo_xO_y, W_xO_y and Ti_xO_y) deposited Cu(111) surfaces are shown in Figure 3.4. For the ^{13}CO TPD result on clean Cu(111) surface, only one peak is observed with a desorption temperature of 165 K. According to previous CO thermal desorption spectra[46], this peak is attributed to the desorption of molecularly bound ^{13}CO molecules. The ^{13}CO TPD results for the metal oxide cluster deposited Cu(111) surfaces do not show any new features. Their peak positions variance range from 163 K to 165 K, which can all attributed to physisorbed ^{13}CO adsorption on Cu(111). The ^{13}CO TPD results show that CO molecules can only physisorb on Cu(111)

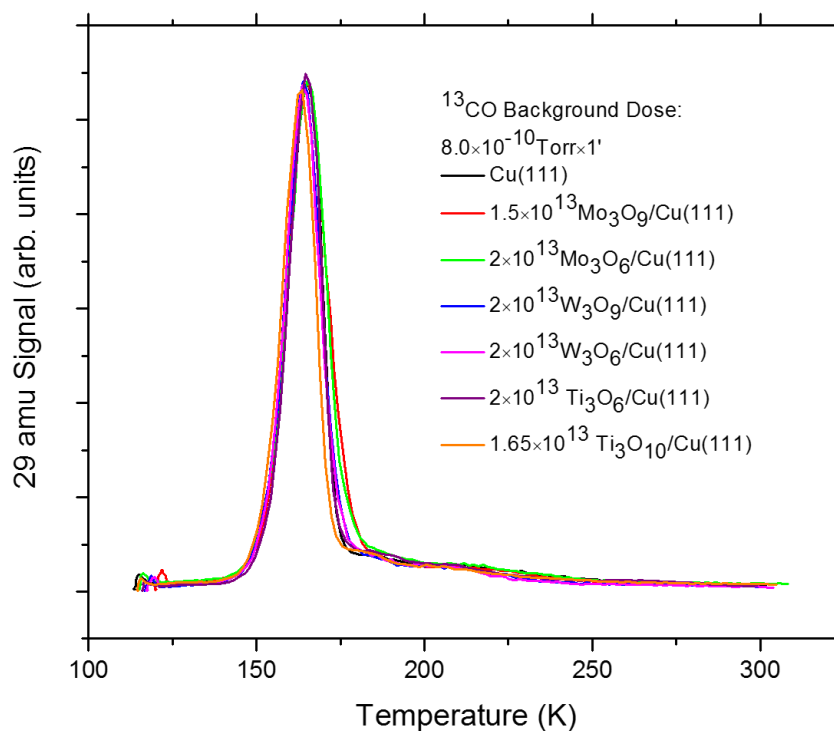**Figure 3.4**: Temperature programmed desorption of ^{13}CO from clean Cu(111) surface and metal oxide cluster (Mo_xO_y, W_xO_y and Ti_xO_y) deposited Cu(111) surface. ^{13}CO was dosed with background pressure of 8.0×10^{-10} Torr for 1 min, which corresponds to 0.048 L.

with no metal oxide cluster-Cu(111) interface related feature. Figure 3.5 shows The D$_2$O TPD spectra of clean Cu(111) surface and metal oxide cluster (Mo$_x$O$_y$, W$_x$O$_y$ and Ti$_x$O$_y$) deposited Cu(111) surface. For the clean Cu(111) surface, the TPD spectra of D$_2$O only show a physisorbed peak at 145 K, which is in agreement with previous water TPD result[47]. After depositing metal oxide clusters onto the Cu(111) surface, the physisorbed D$_2$O peak is generally shifted to a slightly lower temperature by about 1 or 2 K. Moreover, a new broad peak is observed in the range of 170 ~ 178 K. Based on DFT water adsorption calculations[22], this peak is attributed to the D$_2$O adsorption at the cluster-Cu(111) interface or at a metal site in of the metal oxide cluster.
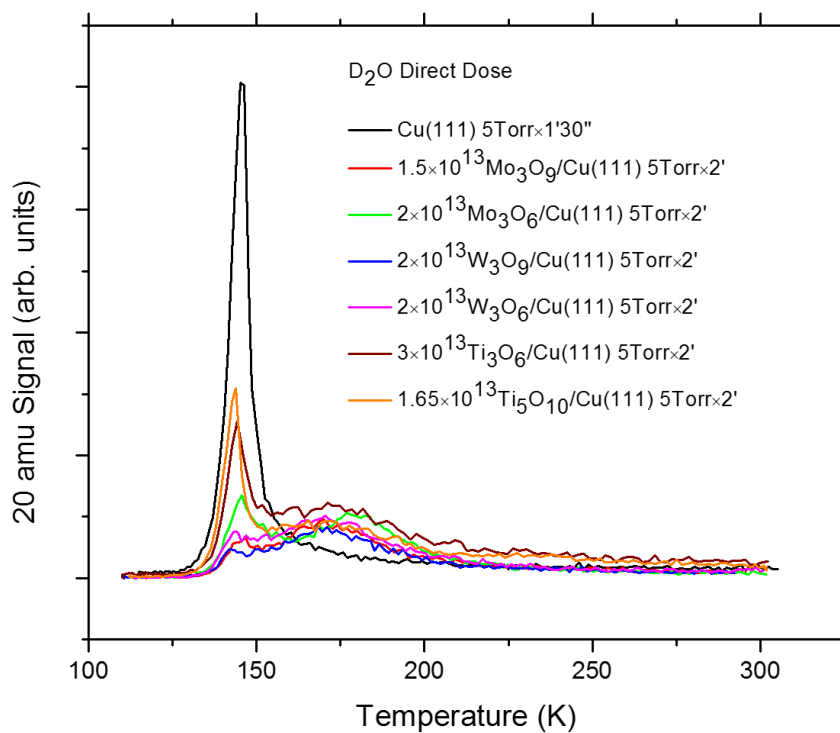
Figure 3.5: Temperature programmed desorption of D_2O from clean Cu(111) surface and metal oxide cluster (Mo_xO_y, W_xO_y and Ti_xO_y) deposited Cu(111) surface. D_2O was directly dosed.

3.4 2PPE Study on Ti_5O_{10} and Ti_3O_6 Clusters Deposited on $Cu_2O/Cu(111)$ Film and Mo_4S_6 Clusters Deposited on $Cu(111)$ Surface

Using an established method[37] introduced in Chapter 2, Section 2.3, Cu_2O film was grown on the $Cu(111)$ surface and monitored with AES and 2PPE spectra, as shown in Figure 3.6. Figure 3.6a shows the AES spectrum of the $Cu_2O/Cu(111)$ film. Both the O KLL peak and Cu peaks are observed, which verifies the oxidation of Cu under our experiment conditions. Figure 3.6b is the 2PPE spectrum of the $Cu_2O/Cu(111)$ film. It displays a new feature around the final state energy of 7.3 eV, which is not observable in the bare $Cu(111)$ 2PPE spectrum. According to the previous report[48], this feature was assigned to be the oxygen induced unoccupied state, which lies 2.8 eV above E_F. In addition, the IS and SS features in the $Cu(111)$ 2PPE spectrum are almost quenched in the $Cu_2O/Cu(111)$ 2PPE spectrum. Based on the 2PPE features, it is further verified that the copper oxide film has been prepared on the $Cu(111)$ surface.

Figure 3.7a shows the work function shifts for Ti_3O_6 and Ti_5O_{10} clusters deposited on both the $Cu_2O/Cu(111)$ film and $Cu(111)$ surface in terms of local cluster coverage. In order to plot the $Ti_3O_6/Cu_2O/Cu(111)$ and $Ti_5O_{10}/Cu_2O/Cu(111)$ work function shift figures, it was assumed that the Ti_xO_y clusters deposited on $Cu_2O/Cu(111)$ have similar radii as those on $Cu(111)$ surface. However, this assumption does not influence the dipole moment calculation using Topping model, because the cluster area falls out during the calculation process. The surface dipole moment of $Ti_3O_6/Cu_2O/Cu(111)$ is calculated to be -2.22 D, whose direction is pointed towards the Cu_2O film. Compared with the surface dipole moment of $Ti_3O_6/Cu(111)$, which is -0.49 D, the surface dipole moment of $Ti_3O_6/Cu_2O/Cu(111)$ is significantly larger. Similar results are also observed for
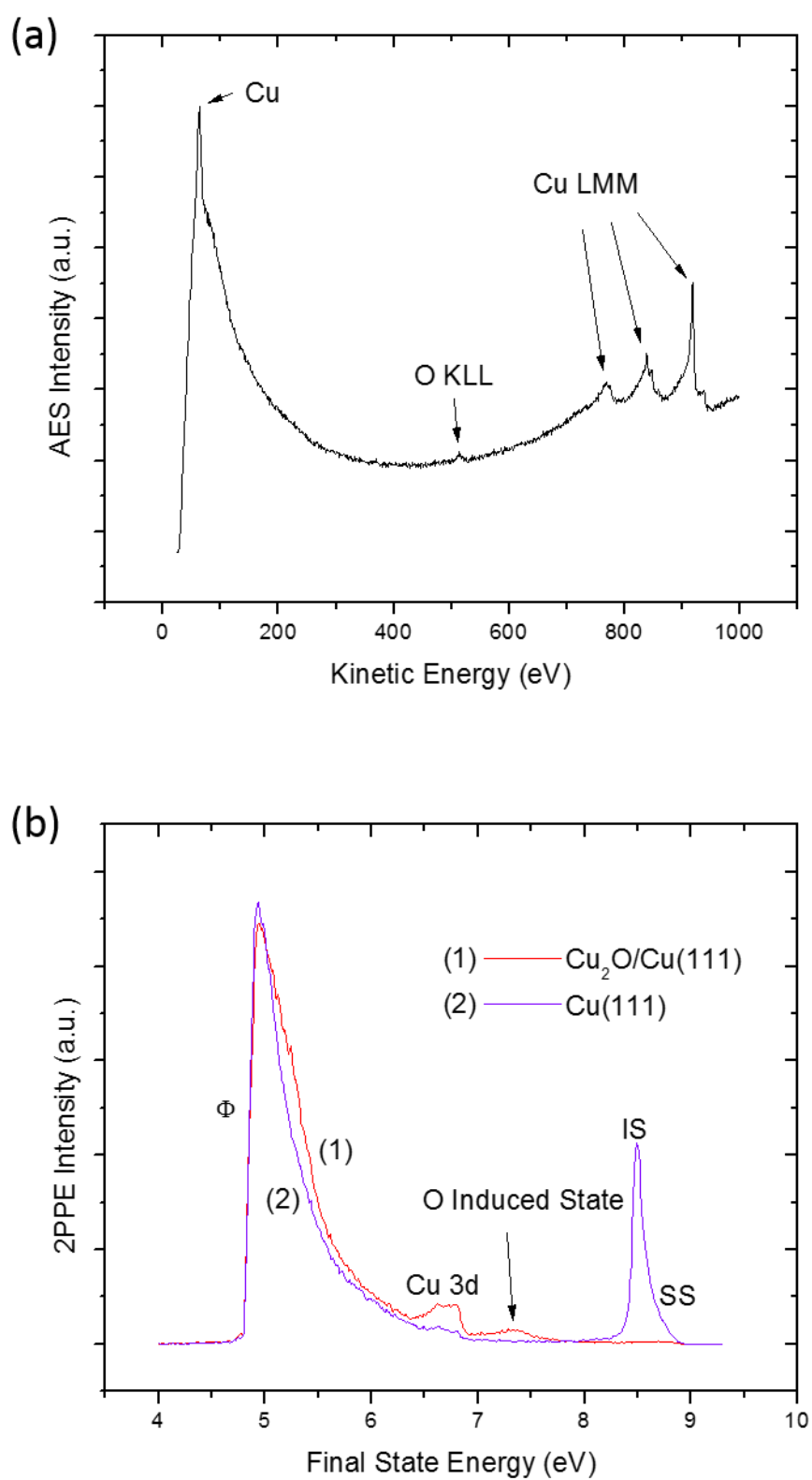
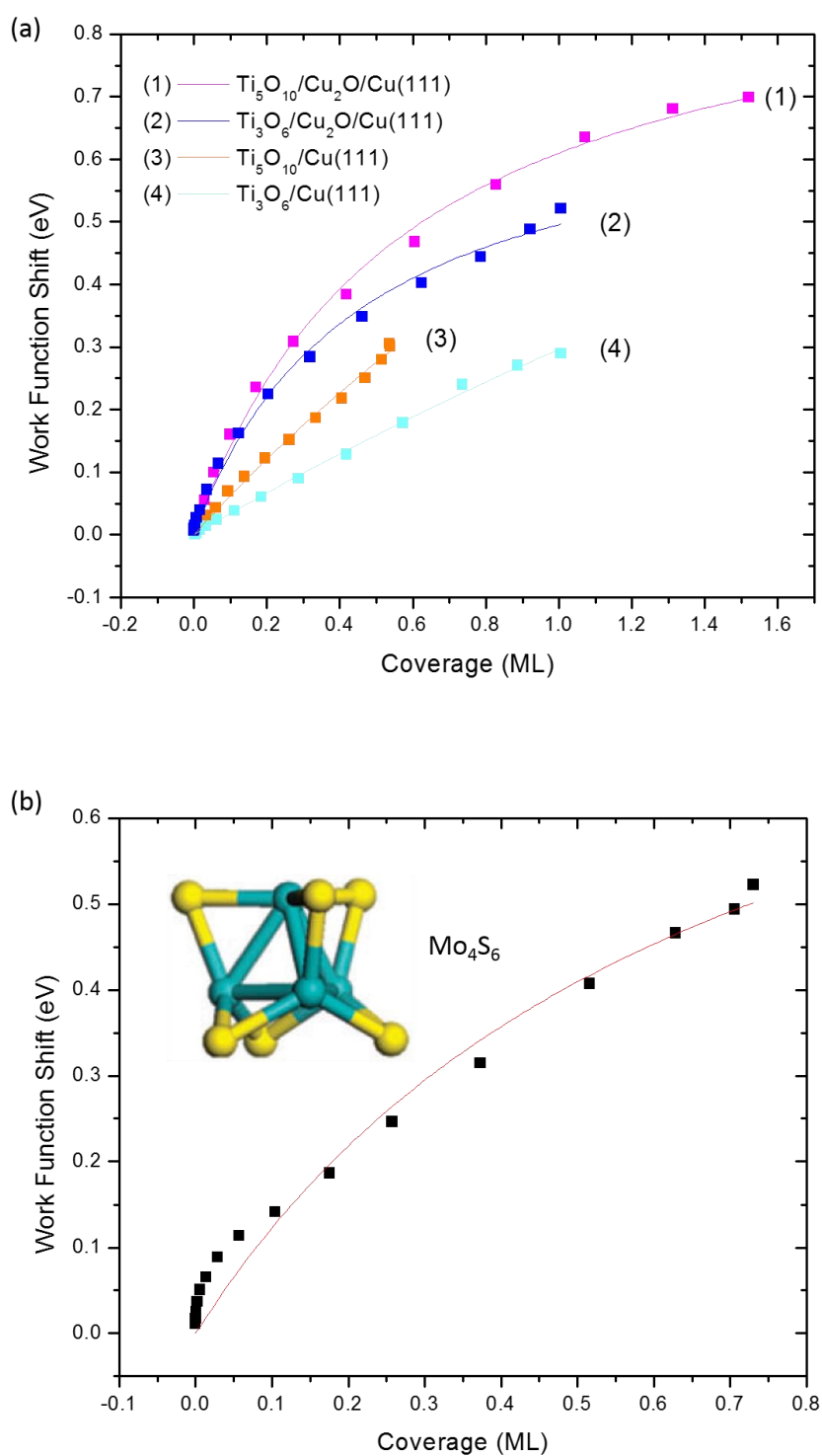**Figure 3.6**: (a) AES spectrum of $Cu_2O/Cu(111)$ film (b) 2PPE spectrum of $Cu_2O/Cu(111)$ film and Cu(111) surface.

Figure 3.7: Work function shift of (a) Ti_xO_y clusters deposited on Cu(111) and Cu_2O/Cu(111) film (b) Mo_4S_6 clusters deposited on Cu(111) surface in terms of local cluster coverage. The optimized DFT gas phase structure is from reference [27].

$Ti_5O_{10}/Cu_2O/Cu(111)$ and $Ti_5O_{10}/Cu(111)$. The calculated surface dipole moments of $Ti_5O_{10}/Cu_2O/Cu(111)$ and $Ti_5O_{10}/Cu(111)$ are -2.52 D and -0.91 D, respectively. It also shows that, by inducing a Cu_2O film between Ti_xO_y clusters and $Cu(111)$ surface, the surface dipole moment will become much larger, which implies strongly enhanced Ti_xO_y cluster-substrate interaction.

In order to explore the interfacial cluster-substrate interaction between metal sulfide and $Cu(111)$, Mo_4S_6 cluster deposited $Cu(111)$ surface was also studied using AES and 2PPE spectroscopic techniques as well as DFT calculations. The optimized DFT gas phase structure of Mo_4S_6 cluster is shown in Figure 3.7b[27]. It displays a highly symmetrical T_d structure, where the four internal molybdenum atoms are located at the tetrahedron corners and surrounded by six bridging sulfur atoms beside the Mo-Mo bonds. Because the DFT structure of the deposited Mo_4S_6 cluster on $Cu(111)$ surface is not available yet, the coverage of deposited Mo_4S_6 clusters is estimated using the gas phase radius of Mo_4S_6 clusters. The work function shift of the Mo_4S_6 cluster deposited $Cu(111)$ surface is plotted in Figure 3.7b in terms of local Mo_4S_6 cluster coverage. The surface dipole moment of $Mo_4S_6/Cu(111)$ from a fit to the data is -1.06 D pointed towards the $Cu(111)$ surface. It is similar to the reported dipole moment value (-1.18 D) of Mo_4S_6 clusters deposited on $Al_2O_3/NiAl(110)$ surface[49]. But the $Mo_4S_6/Cu(111)$ surface dipole moment is smaller than the surface dipole moment of both $Mo_3O_6/Cu(111)$ and $Mo_3O_9/Cu(111)$, which is consistent with their electron affinity order. It might imply a relatively weaker interaction between molybdenum sulfide and $Cu(111)$ surface than that of molybdenum oxide and $Cu(111)$ surface.

3.5 Summary

Using a size-selected cluster deposition apparatus, metal oxide (Mo_3O_9, W_3O_9, Ti_3O_6, Mo_3O_6, W_3O_6, Ti_5O_{10}) and metal sulfide (Mo_4S_6) clusters were made and deposited on a Cu(111) single crystal surface. Ti_3O_6 and Ti_5O_{10} clusters were also deposited on the Cu_2O/Cu(111) film which was made using an established method[37]. The cluster distribution on the substrate is similar for all the systems in this work, where the cluster amount decreases from the center to the deposition edges, as shown by the Gaussian fitting of the AES spectra intensity. The work function shift of the cluster deposited Cu(111) surface and Cu_2O/Cu(111) film becomes larger as the local cluster coverage increases. Using the Topping model, the surface dipole moment was derived in terms of work function shift and all the cluster deposited surface shows the same direction of surface dipole moments, which are pointed towards the substrate. That is associated with the consistent work function shift direction.

For the stoichiometric clusters (Mo_3O_9, W_3O_9, Ti_3O_6) on the Cu(111) surface, Mo_3O_9/Cu(111) and W_3O_9/Cu(111) show a significantly larger dipole moment than Ti_3O_6/Cu(111). These results suggest that charge transfer from Cu(111) surface to metal oxide clusters is less for Ti_3O_6 than that of Mo_3O_9 and W_3O_9. It is also consistent with the electron affinities of these clusters, which are comparable for Mo_3O_9 and W_3O_9, but larger than Ti_3O_6. For the Mo_3O_6 and W_3O_6 clusters with lower metal oxidation states, the electron affinities are smaller and their ability to accommodate more from the Cu(111) surface is reduced, consistent with smaller surface dipole moments. However, Mo_3O_6/Cu(111), W_3O_6/Cu(111) and Ti_3O_6/Cu(111) have very different surface dipole moments from each other, even though they have similar electron affinities. This is thought to be result of different cluster structure and binding patterns on the Cu(111) surface. When the cluster size gets bigger, as in the case of Ti_5O_{10}/Cu(111), more metal

cations are available to accommodate electrons, which can enhance interfacial charge transfer. In the case of Mo_4S_6/Cu(111), the surface dipole moment is much smaller than that of Mo_3O_6/Cu(111) and Mo_3O_9/Cu(111), which is consistent with their relative electron affinities. The surface dipole moment is also slightly smaller than that of Mo_4S_6/Al_2O_3/NiAl(110), which shows a dependence of surface dipole moment on the support. TPD experiments on metal oxide cluster deposited Cu(111) surfaces show similar results with each other, where CO adsorption is not influenced by the cluster deposition while water adsorption shows a new feature in the temperature range of 170 ~ 178 K. This feature is attributed to the water adsorption at the metal site of the metal oxide clusters or the cluster-Cu interface.

Lastly, for the Ti_3O_6 and Ti_5O_{10} clusters deposited on the Cu_2O/Cu(111) film, their work function shifts are larger than corresponding Ti_3O_6/Cu(111) and Ti_5O_{10}/Cu(111) systems. The calculated surface dipole moments for Ti_3O_6/Cu_2O/Cu(111) and Ti_5O_{10}/Cu_2O/Cu(111) are -2.22 D and -2.52 D, respectively, which are significantly larger than that of Ti_3O_6/Cu(111) (-0.49 D) and Ti_5O_{10}/Cu(111) (-0.91 D). The cluster-substrate interaction is much enhanced between Ti_xO_y clusters and the Cu_2O film.

Overall, for the Cu(111)-supported metal oxide clusters with the same elements but different oxidation states, electron affinities can provide a good estimation for the magnitude of surface dipole moment and interfacial charge transfer. For Cu(111)-supported metal oxide clusters with different elements, especially ones with same metal oxidation states, electron affinities should still be taken into consideration as well as the cluster structures, in order to analyze the surface dipole moments and interfacial charge transfer. These results in this thesis shows that the combination of 2PPE and DFT

calculations is powerful in investigating the charge transfer and the interfacial electronic interaction at the cluster-metal interface.

List of References

(1)   Diebold, U. *Surf. Sci. Rep.* **2003**, *48*, 53.

(2)   Giovannetti, G.; Khomyakov, P. A.; Brocks, G.; Karpan, V. M.; van den Brink, J.; Kelly, P. J. *Phys. Rev. Lett.* **2008**, *101*, 026803.

(3)   Koch, N.; Gerlach, A.; Duhm, S.; Glowatzki, H.; Heimel, G.; Vollmer, A.; Sakamoto, Y.; Suzuki, T.; Zegenhagen, J.; Rabe, J. P.; Schreiber, F. *J. Am. Chem. Soc.* **2008**, *130*, 7300.

(4)   Zhang, C.; Yoon, B.; Landman, U. *J. Am. Chem. Soc.* **2007**, *129*, 2228.

(5)   Janssens, T. V. W.; Clausen, B. S.; Hvolbaek, B.; Falsig, H.; Christensen, C. H.; Bligaard, T.; Norskov, J. K. *Top. Catal.* **2007**, *44*, 15.

(6)   Crispin, X.; Geskin, V.; Crispin, A.; Cornil, J.; Lazzaroni, R.; Salaneck, W. R.; Bredas, J. L. *J. Am. Chem. Soc.* **2002**, *124*, 8131.

(7)   Rusu, P. C.; Brocks, G. *J. Phys. Chem. B* **2006**, *110*, 22628.

(8)   Kokalj, A. *Chem. Phys.* **2012**, *393*, 1.

(9)   Haruta, M. *Catal. Today* **1997**, *36*, 153.

(10)   Rodriguez, J. A.; Liu, P.; Wang, X.; Wen, W.; Hanson, J.; Hrbek, J.; Perez, M.; Evans, J. *Catal. Today* **2009**, *143*, 45.

(11)   Yang, Y.; Evans, J.; Rodriguez, J. A.; White, M. G.; Liu, P. *Phys. Chem. Chem. Phys.* **2010**, *12*, 9909.

(12)   Rodriguez, J. A. *Polyhedron* **1997**, *16*, 3177.

(13)   Eck, S.; Castellarin-Cudia, C.; Surnev, S.; Prince, K. C.; Ramsey, M. G.; Netzer, F. P. *Surf. Sci.* **2003**, *536*, 166.

(14)   Hornes, A.; Hungria, A. B.; Bera, P.; Lopez Camara, A.; Fernandez-Garcia,

M.; Martinez-Arias, A.; Barrio, L.; Estrella, M.; Zhou, G.; Fonseca, J. J.; Hanson, J.

C.; Rodriguez, J. A. *J. Am. Chem. Soc.* **2010**, *132*, 34.

(15)   Yan, T.; Redman, D. W.; Yu, W.-Y.; Flaherty, D. W.; Rodriguez, J. A.;

Mullins, C. B. *J. Catal.* **2012**, *294*, 216.

(16)   Gan, L.-Y.; Zhao, Y.-J. *J. Phys. Chem. C* **2012**, *116*, 16089.

(17)   Liu, P. *J. Chem. Phys.* **2010**, *133*.

(18)   Rodriguez, J. A.; Hrbek, J. *Surf. Sci.* **2010**, *604*, 241.

(19)   Haruta, M. *Cattech* **2002**, *6*, 102.

(20)   Heiz, U.; Schneider, W. D. *J. Phys. D: Appl. Phys.* **2000**, *33*, R85.

(21)   Wortmann, B.; Mende, K.; Duffe, S.; Groenhagen, N.; von Issendorff, B.;

Hoevel, H. *Phys. Status Solidi B* **2010**, *247*, 1116.

(22)   Vidal, A. B.; Liu, P. *Phys. Chem. Chem. Phys.* **2012**, *14*, 16626.

(23)   Yang, F.; Choi, Y.; Liu, P.; Stacchiola, D.; Hrbek, J.; Rodriguez, J. A. *J. Am.

Chem. Soc.* **2011**, *133*, 11474.

(24)   Avgouropoulos, G.; Ioannides, T. *J. Mol. Catal. A: Chem.* **2008**, *296*, 47.

(25)   Joly, J. P.; Gaillard, F.; Peillex, E.; Romand, M. *Vacuum* **2000**, *59*, 854.

(26)   Haberland, H.; Karrais, M.; Mall, M.; Thurner, Y. *J. Vac. Sci. Technol., A*

1992, *10*, 3266.

(27)   Lightstone, J. M.; Patterson, M. J.; White, M. G. *Chem. Phys. Lett.* **2005**, *413*,

429.

(28)   Batey, J. H. *Vacuum* **1987**, *37*, 659.

(29)   Jones, R. M.; Anderson, S. L. *Rev. Sci. Instrum.* **2000**, *71*, 4335.

(30)   Busolt, U.; Cottancin, E.; Rohr, H.; Socaciu, L.; Leisner, T.; Woste, L. *Eur. Phys. J. D* **1999**, *9*, 523.

(31)   Redhead, P. A. *Vacuum* **1962**, *12*, 203.

(32)   Szymanski, P.; Garrett-Roe, S.; Harris, C. B. *Prog. Surf. Sci.* **2005**, *78*, 1.

(33)   Petek, H.; Ogawa, S. *Prog. Surf. Sci.* **1997**, *56*, 239.

(34)   Gartland, P. O.; Berge, S.; Slagsvol, B. J. *Phys. Rev. Lett.* **1972**, *28*, 738.

(35)   Lindgren, S. A.; Wallden, L. *Phys. Rev. B* **1980**, *22*, 5967.

(36)   Settle, F. A. *Handbook of instrumental techniques for analytical chemistry*, Prentice Hall PTR, Upper Saddle River, NJ, **1997**.

(37)   Yang, F.; Choi, Y. M.; Liu, P.; Hrbek, J.; Rodriguez, J. A. *J. Phys. Chem. C* **2010**, *114*, 17042.

(38)   Childs, K. D.; Hedberg, C. L. *Handbook of Auger electron spectroscopy : a book of reference data for identification and interpretation in Auger electron spectroscopy*, Physical Electronics Inc., Eden Prairie, Minn., **1995**.

(39)   Wang, H. F.; Dutton, G.; Zhu, X. Y. *J. Phys. Chem. B* **2000**, *104*, 10332.

(40)   Hertel, T.; Knoesel, E.; Hasselbrink, E.; Wolf, M.; Ertl, G. *Surf. Sci.* **1994**, *317*, L1147.

(41)   Huang, X.; Zhai, H. J.; Kiran, B.; Wang, L. S. *Angew. Chem. Int. Ed.* **2005**, *44*, 7251.

(42)   Zhai, H.-J.; Wang, L.-S. *J. Am. Chem. Soc.* **2007**, *129*, 3022.

(43)   Rothgeb, D. W.; Mann, J. E.; Waller, S. E.; Jarrold, C. C. *J. Chem. Phys.* **2011**, *135*.

(44)   Topping, J. *Proc. R. Soc. London, A* **1927**, *114*, 67.

(45)   Pivetta, M.; Patthey, F.; Schneider, W. D.; Delley, B. *Phys. Rev. B* **2002**, *65*, 045417/1.

(46)   Kirstein, W.; Kruger, B.; Thieme, F. *Surf. Sci.* **1986**, *176*, 505.

(47)   Hinch, B. J.; Dubois, L. H. *J. Chem. Phys.* **1992**, *96*, 3262.

(48)   Wei, W.; White, J. M. in *Physical Chemistry of Interfaces and Nanomaterials III, Vol. 5513* (Eds.: G. V. Hartland, X. Y. Zhu), Spie-Int Soc Optical Engineering, Bellingham, **2004**, pp. 157.

(49)   Zhou, J.; Zhou, J.; Camillone, N., III; White, M. G. *Phys. Chem. Chem. Phys.* **2012**, *14*, 8105.